scientific reports

Check for updates

OPEN

Investigation of the nanostructure and nanomechanical properties of the interphase in carbon fiber reinforced polyamide-6 composite

Yixin Qi[1,2]✉, Dazhi Jiang[2,3], Su Ju[2] & Jianwei Zhang[2]

Carbon fiber reinforced polyamide-6 (CF/PA-6) composites have been widely applied in automobile, aerospace, and biomedical industries for their high mechanical properties, high thermal resistance and recyclability. On the purpose of finding ways to improve the interfacial properties, the investigation of the nanostructure and nanomechanical properties of the interphase in CF/PA-6 composites were essential. In this study, MD simulation was carried out to show the interfacial formation and nanostructure of the CF/PA-6 composite model directly at the atomic level and compute the radial distribution function, interfacial energy, total energy. Then the nanomechanical properties of the CF/PA-6 composite, such as interfacial thickness, interfacial modules, interfacial adhesion, were investigated by AFM PF-QNM model. The changes of the radical distribution function and energies over the MD simulation time indicated that the PA-6 chains adsorbed and then regularly folded on the CF surface, displaying the interfacial crystallization of the CF/PA-6 composite model. What stood out in the AFM PF-QNM tests were the abrupt decreasing of the interfacial modulus and the sharp increasing of the interfacial adhesion from those of the carbon fiber to those of the PA-6. The average interfacial thickness of the CF/PA-6 composite was 72 nm. Consistent with the simulation results, the interfacial properties were distinct from the properties of the carbon fiber and PA-6, owning to the adsorption and orderly folding of the PA-6 chains on the CF surface and the changes of the RDF and energies.

Keywords Interfacial thickness, Peakforce quantitative nanomechanical, Molecular dynamics simulation, Carbon fiber reinforced polyamide-6 composite

Carbon fiber reinforced polyamide-6 (CF/PA6) composites have attracted worldwide attention for their high mechanical properties, high thermal resistance, recyclability and cost-effective processing[1]. However, the commercial CF is generally not easy to bond well with the PA6 because of the thermosetting sizing agent coating on surface[2]. Meanwhile, the high processing viscosity of the PA6 makes it difficult to permeate the CF sufficiently, resulting in voids and dry spots in the interphase[3,4]. As interphase acts as a "bond" to transfer stress from matrix to reinforcement, it is vital to investigate and improve the interfacial structure and property of CF/PA6 composites, which determine the mechanical properties[5,6].

Aim to find ways to improve the mechanical properties of CF/PA6 composites, the investigation of the interfacial structure is essential. Methods of studying the interfacial structure involved scanning electron microscopy (SEM)[7–9], X-ray diffractometer (XRD)[7], X-ray photoelectron spectroscopy (XPS)[8,9], polarizing microscope (PM), differential scanning calorimeter (DSC)[7,9,10], have been widely used[11]. Petrény et al.[7] investigated the interphase formed around the carbon nanotubes and carbon fibers with a polyamide-6 matrix, the DSC curves and XRD patterns revealed that the crystallites grew epitaxially on the surface of the carbon nanotubes, resulting in decreased average crystallite size in the composites, and the larger interphase fraction in the composites led to better mechanical performance. Sun et al.[8] introduced 20 wt% precursor solution coating on the CF surface by in-situ anionic ring-opening polymerization, the SEM images showed that the PA6 resin was deeply embedded in the groove of CF in CF/PA6-20 composites, and the fracture of PA6 droplet was irregular and showed a ductile fracture.

[1]School of Materials Science and Engineering, North University of China, Taiyuan 030051, China. [2]College of Aerospace Science and Engineering, National University of Defense Technology, Changsha 410073, China. [3]School of Materials, Sun Yat-Sen University, Guangzhou 510275, China. ✉email: qyx546024729@sina.com

The above researches mostly centre around the crystallite and fracture morphology of the interphase in CF/PA6 composites. To explore the nanostructure of the interphase directly, an increasing effective method, atomic force microscope (AFM) peakforce quantitative nanomechanical (PF-QNM) mode, is used to calculate the interfacial thickness, interfacial modulus and interfacial adhesion[11–14]. Molecular dynamics (MD) simulation is a intuitive way to observe the interfacial formation and compute the radial distribution function (RDF), interfacial energy, total energy at the atomic scale[15–19]. Khalil et al.[20] found that the average interfacial thickness in desized CF/PP composites by PF-QNM was 84.17% higher (212.9 ± 21 nm) as compared to 115.6 ± 21 nm in sized CF/PP composites. Wang et al.[21] uncovered a notable shift in the failure mode of CF/PA6 composites under uniaxial tensile loading through MD simulation. It was observed that increasing loading temperatures led to the deterioration of the mechanical properties of PA6, resulting in a gradual transition of the primary failure mode from adhesive failure to cohesive failure.

So far, few research reports the nanostructure and nanomechanical properties of the interphase in CF/PA6 composites. Therefore, in this study, in order to provide a useful guide for the improvement of the interfacial and mechanical properties, the nanostructure and nanomechanical properties of the interphase in CF/PA6 composite were tested by PF-QNM mode and MD simulation. The PF-QNM mode by AFM of the CF/PA6 composite was carried out to exactly evaluate the interfacial thickness, interfacial modulus and interfacial adhesion[14,22–24]. Moreover, the interfacial formation, radial distribution function, interfacial energy, total energy were evaluated using MD simulation[25–28].

Simulations and experiments

Models and simulation methods

All models and simulations in this work were performed using the Materials Studio (Accelrys Inc) software to view the interfacial formation and analyse the interfacial structure in an atomic scale. We first built a PA6 chain (100 $C_6H_{11}NO$) and a 2-layer graphene with 10 –COOH groups and 99 –COOH groups. Then, we constructed 2 PA6 chains in a maximum contact with the 2-layer graphene surface in one model (CF/PA6 composite model), whose dimensions were 34.36 Å × 39.36 Å × 46.80 Å (Fig. 1). After, geometry optimization and anneal tasks were carried out on the CF/PA6 composite model to gain the optimal structure with minimum energy. Lastly, in simulation process, a 2000 ps dynamics NVT was applied to simulate the formation of the interphase, that was the dynamic of the PA6 chains on the CF surface[29]. The force field employed for the CF/PA6 composite model is COMPASSII, the charges is forcefield assigned. All input and control parameters for the simulations were listed in Table 1.

How density varies as a function of distance from a reference particle is defined as radical distribution function (RDF)[28,29]. The RDF *g(r)* can be expressed as

$$g(r) = \rho(r) / \rho_{total} = \left(N \Big/ \frac{4}{3}\pi\left((r+dr)^3 - r^3\right) \right) \Big/ \rho_{total} \tag{1}$$

where r is the distance from the reference particle, $\rho(r)$ is the the average particle density between r and $r+dr$, ρ_{total} is the total particle density, N is the number of the particles between r and $r+dr$[27,29]. For crystalline and semi-crystalline polymer, the RDF $g(r)$ shows the distribution characteristics of the surrounding environment of a particle and characterizes its short-range order.

The total energy E_{total} describes the potential energy surface of a particular structure as a function of its atomic coordinates, can be expressed as s sum of valence (or bond), cross term, and non-bond interactions[29]:

$$E_{total} = E_{valence} + E_{crossterm} + E_{non-bond} \tag{2}$$

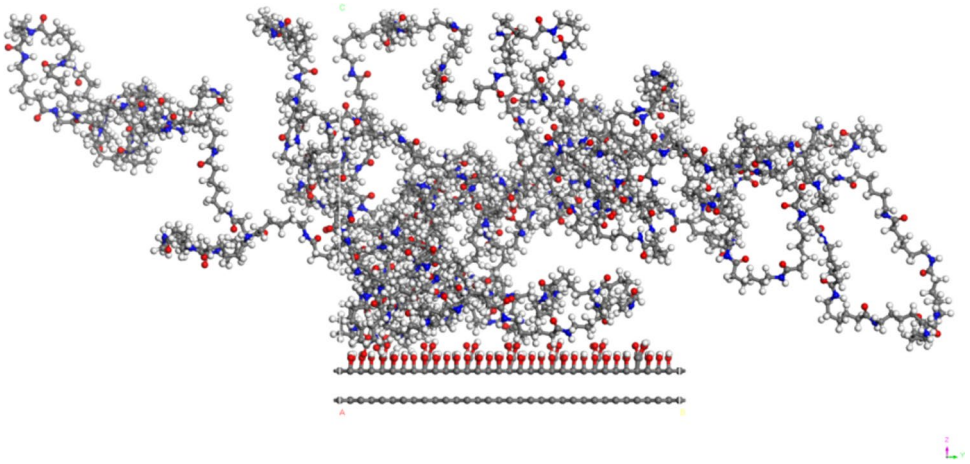

Figure 1. The structure of the CF/PA6 composite model.

Simulation process	Input and control parameters
Geometry optimization	Algorithm: smart
	Energy tolerance: 0.00002 kcal/mol
	Force tolerance: 0.001 kcal/mol/Å
	Maximum iteration: 500
Anneal	Number of anneal cycles: 5
	Initial temperature: 300 K
	Heating ramps per cycle: 5
	Dynamics steps per ramp: 100
	Ensemble: NVT
	Control method: nose
	Timestep: 1.00 fs
	Van Der Waals cutoff distance: 18.5 Å
Dynamics in simulation process	Ensemble: NVT
	Temperature: 300K
	Control method: nose
	Timestep: 1.00 fs
	Total simulation time: 2000 ps
	Van Der Waals cutoff distance: 12.5 Å

Table 1. All input and control parameters for the simulations.

where $E_{valence}$ is the valence energy, like bond stretching, valence angle bending, dihedral angle torsion. $E_{crossterm}$ is the crossterm energy, such as tretch-stretch, stretch-bend-stretch, bend-bend, torsion-stretch. $E_{non\text{-}bond}$ is the non-bond enregy, as van der Waals, electrostatic[26,29].

Interfacial energy of polymer composite is usually hard to test directly, therefore MD simulation is widely used to compute the interfacial energy in theory[29]. The interfacial energy $E_{interaction}$ is represented as

$$E_{interaction} = E_{total} - E_{polymer} - E_{surface} \tag{3}$$

where E_{total} is the model total energy, $E_{polymer}$ is the model total energy without reinforcement, $E_{surface}$ is the model total energy without polymer[28,29].

Experiments

Materials

The polyamide-6 (PA6) and unidirectional carbon fiber reinforced PA6 prepreg sheet used in this study was supplied by composites Inc. The abrasive papers were Eagle Brand waterproof from Japan. The nano-alumina particles (0.5 μm, 0.05 μm) were provided by Shagnhai Naibo Inc. The polymethylmethacrylate resin system (HY604-Y) was offered by Zhejiang Wuyi Hengyu Instrument Inc.

DSC analysis

Aim to gain the melting range of the PA6, non-isothermal DSC tests (Mettler Toledo DSC1) were carried out. The PA6 particles were first heated form 25–270 ℃ at a rate of 10 ℃/min, after keeping 5 min at 270 ℃, cooling to 190 ℃ at the same rate of 10 ℃/min and staying for 5 min to eliminate thermal history. Then a heating process from 190 to 270 ℃ at a rate of 10 ℃/min was conducted on the PA6 particles, which showed the melting process of the PA6 particles. In the end, cooling to the room temperature, and the weight of the PA6 particles were recorded.

Figure 2A and B presented the heat flow/time/temperature curves of the PA6, it was apparent that the area of the endothermic melting peak of eliminating thermal history was bigger, compared to that of melting process. Therefore, eliminating thermal history was vital for testing the melting range. The melting process which was circled in blue in Fig. 2B was blown up in Fig. 2C. As could be seen from the figure, the melting range of the PA6 was 200.1–230.0 ℃, and it was crystalline polymer. Before and after the DSC test, the weight of the PA6 almost did not change, meaning that there was no chemical reaction during the melting process.

Rheological analysis

To determine forming process, the rheological properties of the PA6 were measured with a rheometer (HAAKE MarsIII) using two parallel plates (20 mm diameter, smooth surface). First of all, Oscillatory model was carried out with a constant frequency of 1 Hz at 240 ℃ while the strain increased from 0.05 to 5%. The result in Fig. 3 presented that the storage modulus G′ and loss modulus G″ of the PA6 remained constant when the strain was 1%, which was the best choice for the following viscosity test[30]. Then, the PA6 particles were heated and pressed within the two parallel plates to a lamina at 250 ℃, cooling to 210 ℃ and keeping 20 min to eliminate thermal history[31]. With a constant frequency of 1 Hz and a strain of 1%, the PA6 lamina was heated again from 210 to 270 ℃ at a rate of 5 ℃/min to gain the viscosity/temperature curve, as showed in Fig. 4A. It was apparent that the viscosity of the PA6 decreased steeply with the increasing temperature, and became flat at 248 ℃. Therefore,

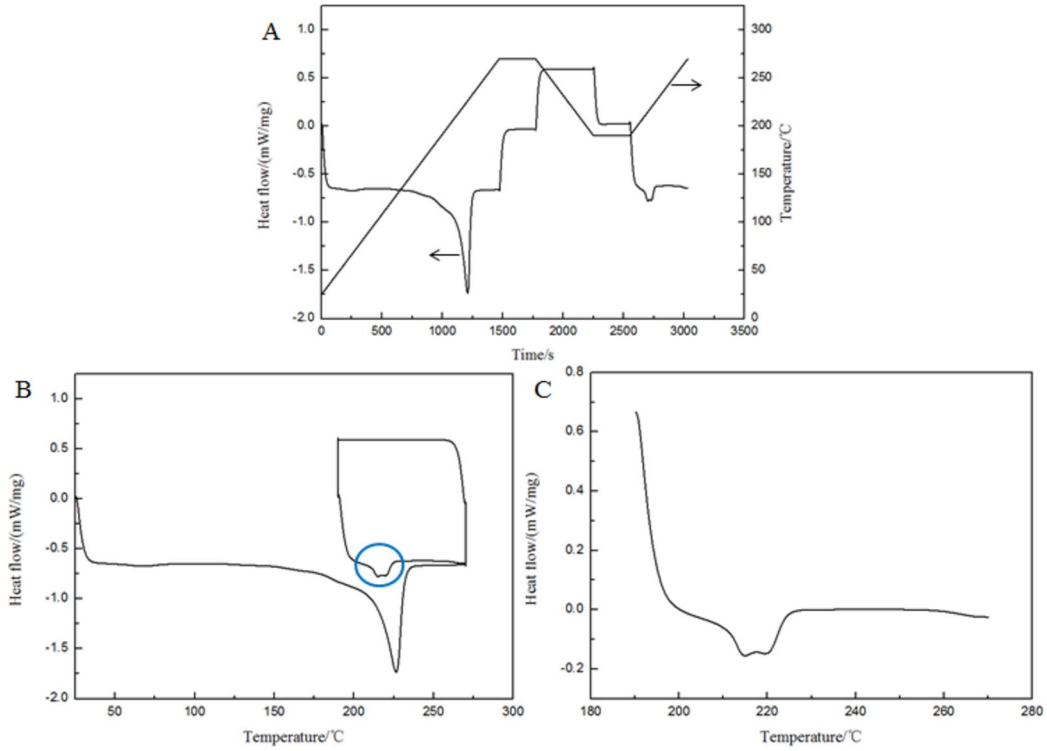

Figure 2. Representative DSC curves of the polyamide-6: (**A**) representative heat flow/time/temperature curve, (**B**) representative heat flow/temperature curve, (**C**) corresponding heat flow/temperature curve of the blue circle in (**B**).

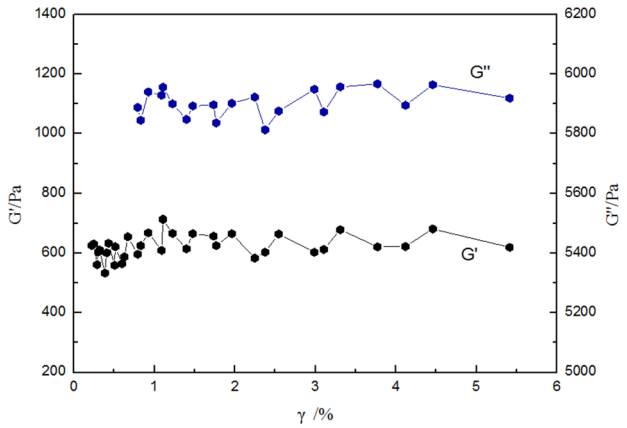

Figure 3. The storage modulus G′/loss modulus G″/strain curve of the polyamide-6.

the forming process could be heating the PA6 from 30 to 250 ℃ at a rate of 5 ℃/min and staying for 15 min[30,31]. In the end, Fig. 4B displayed the viscosity/temperature curve of the PA6 during the hot pressing process. The viscosity of the PA6 was about 100,000 mPa s at 250 ℃, which was conducive to the flowing and impregnation of the PA6 in the CF/PA6 composite during the hot pressing process.

Preparation of PF-QNM samples

The CF/PA6 composite was produced by unidirectional carbon fiber reinforced PA6 prepreg sheet via the hot pressing technology. Ten layers of the prepreg sheets with the same length and width of 200 mm were heated from 30 to 250 ℃ at a rate of 5 ℃/min and stayed for 15 min under 1 MPa. The dimensions of the CF/PA6 composite by hot pressing technology were 200 mm × 200 mm × 2.1 mm, and there were few defects such as bubbles, holes and micro-cracks on its surface. Then, the CF/PA6 composite was cut to cubes with the approximate dimensions of 15 mm × 5 mm × 2.1 mm. And the cubes were embedded in the polymethylmethacrylate resin system (HY604-Y)

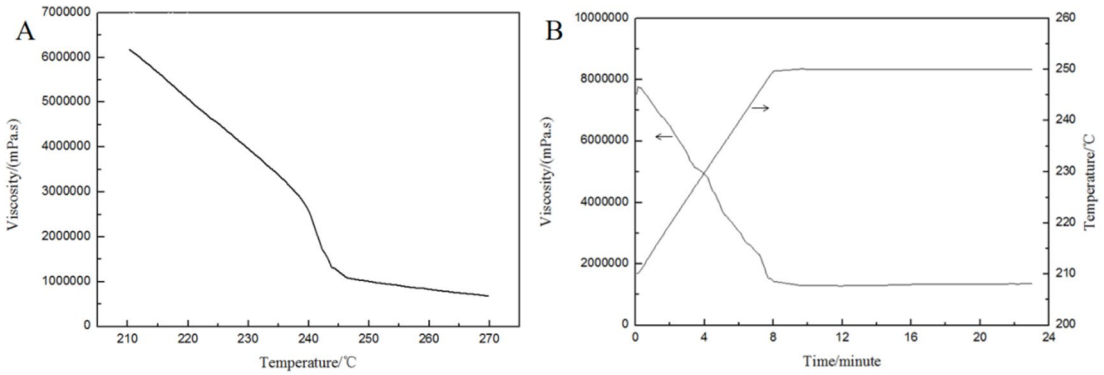

Figure 4. (**A**) The viscosity/temperature curve of the polyamide-6, (**B**) the viscosity/time/temperature curve of the polyamide-6 in the hot pressing process.

in a hollow soft cylindrical mold and cured at room temperature for an hour, these cured samples had carbon fibers orienting along the upright axis perpendicular to the top and bottom surfaces[32,33]. The surface of the samples were ground mechanically with abrasive papers and polished with nano-alumina particle suspension. After being cleaned in an ultrasonic cleaner and dried by a hairdryer, the PF-QNM samples were prepared already.

PF-QNM tests

To determine the nanostructure of the interphase in the CF/PA-6 composites, the interfacial thickness, interfacial modulus and interfacial adhesion were studied in PF-QNM mode by a Bruker Dimension R Icon™ AFM. All quantitative measurements were carried out with an Bruker probe at 512 × 512 pixel resolution, whose Poisson's ratio was 0.3, vibrational frequency was 1 kHz[32,34]. The cantilever spring constant and probe tip radius were calibrated by a polystyrene film (2.7 GPa). In the tests, the probe tip approached and retracted from the surface of the PF-QNM samples repeatedly to capture the height, modulus and adhesion images by acquiring and analyzing force-separation curves simultaneously. The PF-QNM samples' Young's modulus E^* is calculated by

$$E^* = \left[\frac{1-\nu_t^2}{E_t} + \frac{1-\nu_s^2}{E_s}\right]^{-1} \tag{4}$$

where E_t and E_s are the Young's modulus of the probe tip and PF-QNM sample, ν_t and ν_s are the Poisson's ratio of the probe tip and PF-QNM sample, respectively[32]. The adhesion is given by

$$F_{tip} = \frac{4}{3}E^*\sqrt{Rd^3} + F_{adh} \tag{5}$$

where F_{tip} is the force applied on the probe tip, E^* is the Young's modulus, R is the probe tip radius, d is the instantaneous deformation of the PF-QNM sample, F_{adh} is the adhesion[32,35].

Results and discussions

MD simulation results and discussions

Radical distribution function

Figure 5 presented the changes of the PA-6 chains on the CF surface in the CF/PA-6 composite model during 2000 ps dynamics NVT, simulating the interfacial formation. It was somewhat interesting that the PA-6 chains adsorbed to the CF surface closely from 0 to 100 ps, and then folded orderly and tightly on the CF surface from 100 to 1000 ps, which could be the process of the interfacial crystallization. To exactly characterize the short-range order of the CF/PA-6 composite model, the radical distribution function (RDF), which quantitatively presented the distribution characteristics of the H atoms of the PA-6 chains, was computed in Fig. 6. At 0 ps, the H atoms spread randomly near the CF surface from 2 to 74 Å, so did the RDF *g(r)*. Until 100 ps, two distinct peaks of the RDF *g(r)* started to appear at around 12, 20 Å, and the distribution of the RDF *g(r)* shrunk to 0–69 Å, because of the tight approach of the H atoms of the PA-6 chains on the CF surface. At 2000 ps, three peaks of the the RDF *g(r)* occurred at about 7, 13, 21 Å, attributing to the regular folding of the PA-6 chains on the CF surface. Moreover, it was intriguing that the PA-6 chains seemed to fold layer by layer. In a word, the PA-6 chains firstly adsorbed and secondly regularly folded on the CF surface over the simulation time, presenting the crystallization of the interphase of the CF/PA-6 composite.

Total energy and interfacial energy

As the simulation time increased, the total energy of the CF/PA-6 composite model reduced in Fig. 7A, seeking to reach a stable status with lowest total energy. From 0 to 100 ps, the total energy decreased keenly, valence interactions and non-bond interactions accounted for about 45% and 35% of the decreasing respectively, as shown in Fig. 7B. The valence interactions is generally accounted for by diagonal terms, such as bond stretching, valence angle bending, dihedral angle torsion. The non-bond interactions between non-bonded atoms is accounted for by van der Waals, electrostatic. Thus, the adsorption of the PA-6 chains on the CF surface dominated from 0 to

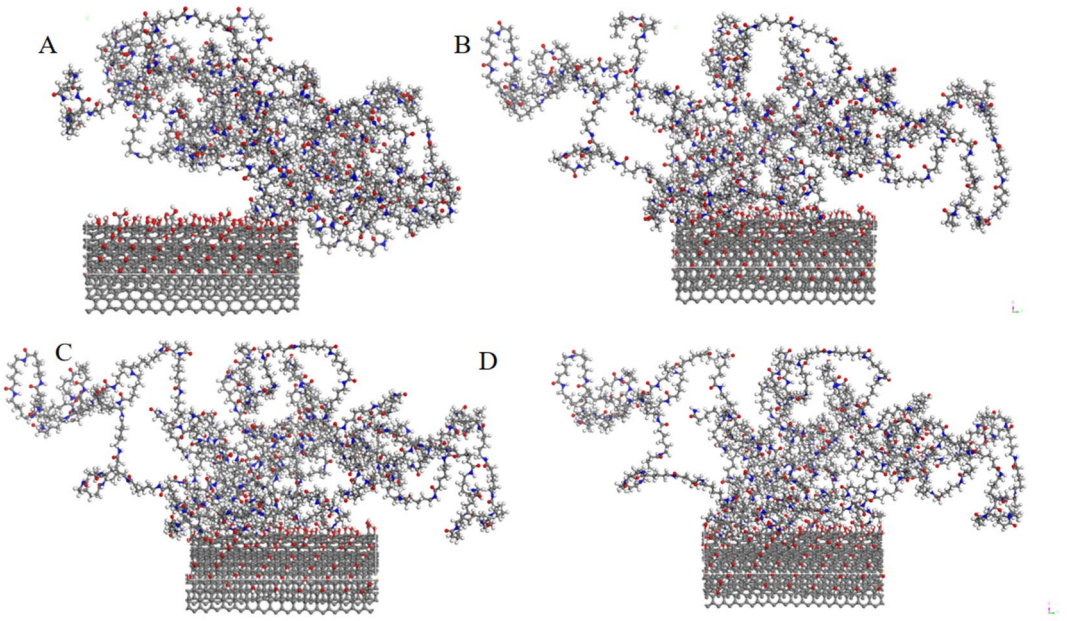

Figure 5. The changes of the PA-6 chains on the CF surface in the CF/PA-6 composite model during the simulation process, (**A**) 0 ps, (**B**) 100 ps, (**C**) 500 ps, (**D**) 1000 ps.

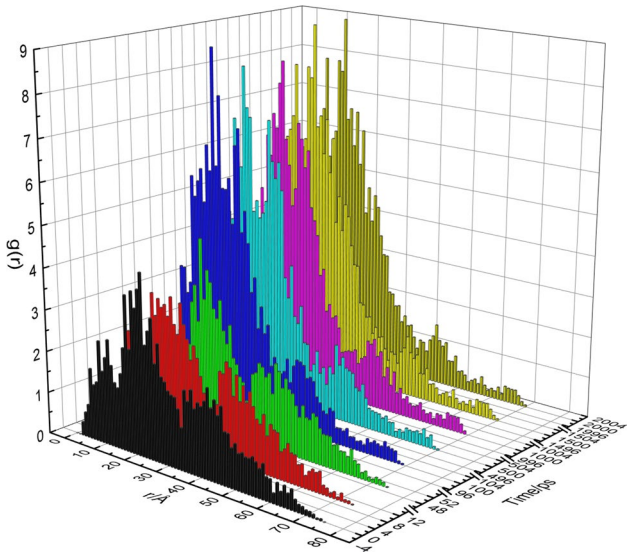

Figure 6. The Radical distribution function RDF *g(r)* of the CF/PA-6 composite model during the simulation process.

100 ps. However, as the PA-6 chains folded regularly and crystallized, the total energy reduced slowly from 100 to 2000 ps, the decreasing of valence energy reduced, the decreasing of non-bond energy and crossterm energy increased. Cross terms are account for such factors as bond or angle distortions caused by nearby atoms. The energy of interactions between non-bonded atoms is accounted for by van der Waals, hydrogen bond terms in some older forcefields. Because of the orderly folding of the PA6 chains on the CF surface, the effects of the non-bond energy and crossterm energy increased from 100 to 2000 ps. At 2000 ps, the total energy was lowest, and the CF/PA-6 composite model reached a stable status.

In Fig. 8, the interfacial energy between the carbon fiber and PA-6 in the CF/PA-6 composite model decreased with the increasing simulation time. Specially, the interfacial energy reduced sharply from 0 to 100 ps, which could be the absorption step of the PA-6 chains on the CF surface. From 100 to 2000 ps, the interfacial energy decreased slowly, attributing to the regular folding of the PA-6 chains on the CF surface. The interfacial energy was lowest at 2000 ps, indicating the strongest interactions between the PA-6 chains and CF surface.

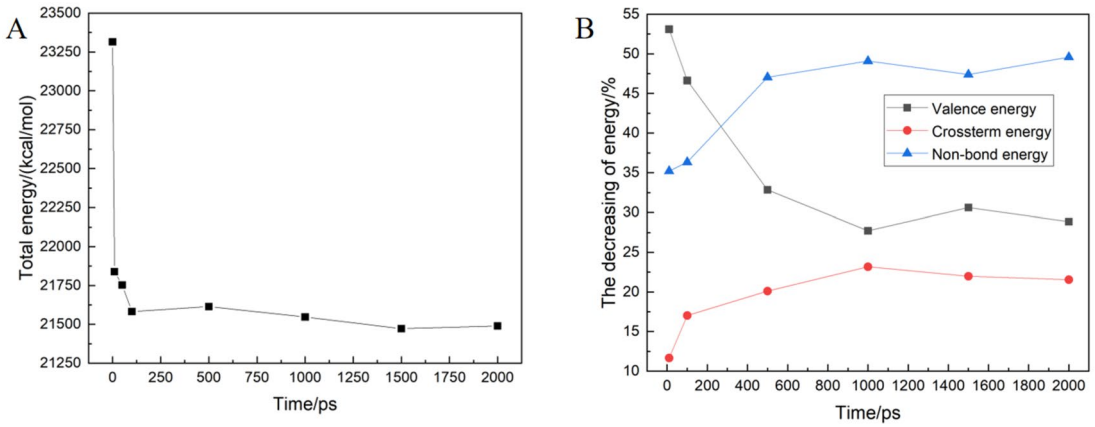

Figure 7. (**A**) The total energy of the CF/PA-6 composite model during the simulation process, (**B**) the decreasing of valence energy, crossterm energy and non-bond energy of the CF/PA-6 composite model during the simulation process.

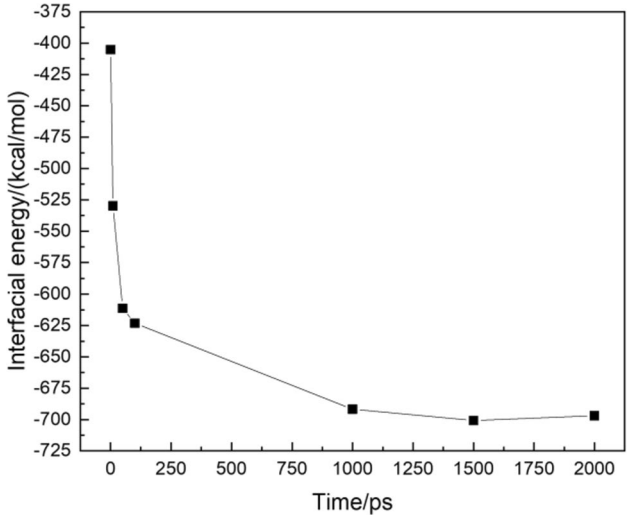

Figure 8. The interfacial energy of the CF/PA-6 composite model during the simulation process.

In conclusion, all simulation results were always consistently, the adsorption and orderly folding of the PA-6 chains on the CF surface, were the two steps of the interfacial formation in the CF/PA-6 composite model. The special crystallization of the interphase resulted in particular interfacial properties of the CF/PA-6 composite.

PF-QNM results and discussions

Height

Figure 9A displayed the typical PF-QNM height image of the surface of the PF-QNM sample, the light circle region was the carbon fiber, the darker part around was the PA-6, and the distinctly darkest boundary region between them was the interphase. The different color reflected the change of height, the darker the color, the lower the height. It was apparent that the interphase was the lowest region among them. In Fig. 9B, the height data of a radial scanning line in Fig. 9A was given. From the height data, nanoscale pits and grooves were observed, which proved that the surface of the PF-QNM sample was smooth enough for tests and had little effect on the results[33].

Modulus and interfacial thickness

The representative PF-QNM modulus image of the interphase of the CF/PA-6 composite was shown in Fig. 10A, the different color indicated the magnitude of the modulus. What stood out in the figure was the marked difference between the modulus of the carbon fiber and PA-6, the light circle region was the carbon fiber with high modulus, the darker part around was the PA-6 with lower modulus, and the boundary region between them was the interphase. In Fig. 10B, the PF-QNM 3D modulus image directly displayed the sharp decreasing of the modulus of the interphase from that of the carbon fiber to that of PA-6. In accordance with the simulation results, the interfacial properties were distinct from the properties of the carbon fiber and PA-6, attributing to the special crystallization of the interphase. To gain exact modulus data of the interphase, a radial scanning line

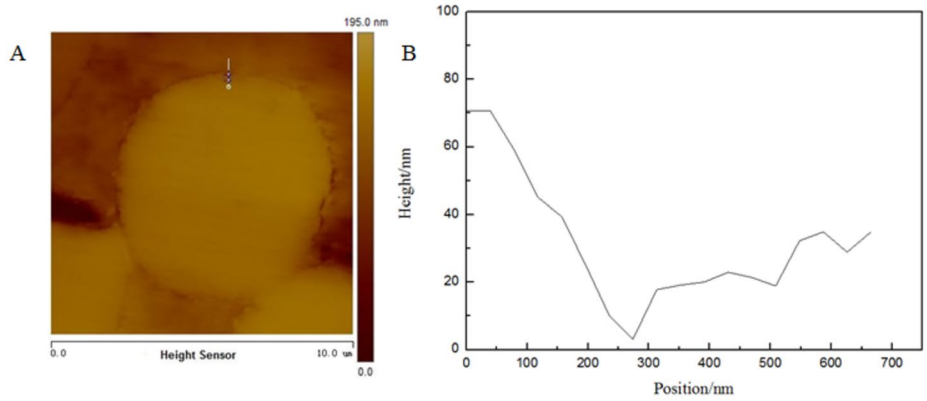

Figure 9. The typical PF-QNM height image of a CF/PA-6 composite sample: (**A**) the height image, (**B**) corresponding data of the radial scanning line in (**A**).

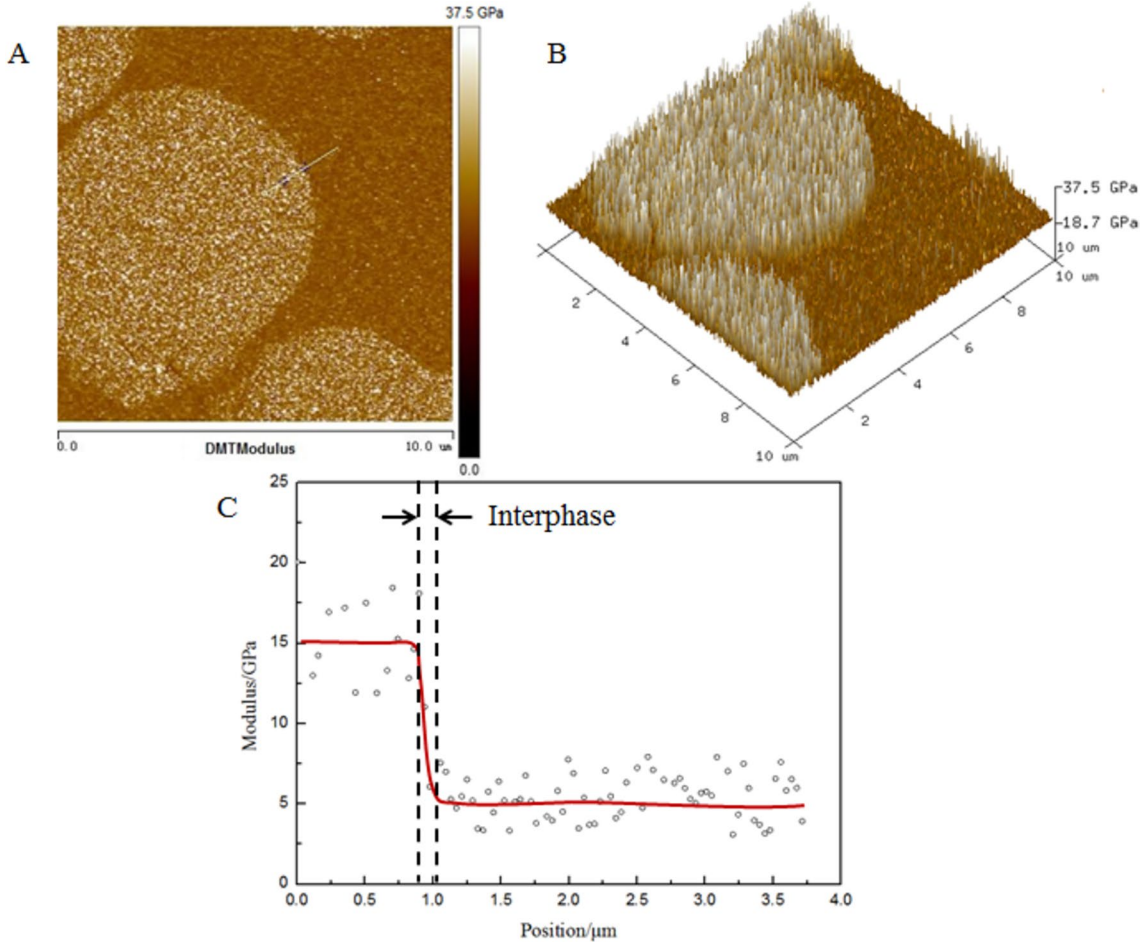

Figure 10. The representative PF-QNM modulus image of the CF/PA-6 composite sample by hot pressing molding: (**A**) the PF-QNM modulus image, (**B**) the PF-QNM 3D modulus image, (**C**) corresponding data of the radial scanning line in (**A**).

from the carbon fiber to the PA-6 in Fig. 10A was taken, the corresponding modulus data of the line was represented in Fig. 10C. According to the modulus data, the modulus of the carbon fiber in the CF/PA-6 composite was about 12–18 GPa, which was clearly lower than the normal value because the probe used was chosen based on the modulus of the PA-6. While the modulus of the PA-6 was normal, about 2.5–7.5 GPa[32]. After fitting the scattered modulus data, as red curve shown in Fig. 10C, we defined the 90% of the width of the decreasing modulus region in the fitting curve as the interfacial thickness of the CF/PA-6 composite[33]. Table 2 displayed

	Interfacial thickness (nm)	Average (nm)	CV (%)
CF/PA-6 composite	78.4, 71.1, 70.4, 70.4, 71.4, 74.7, 70.3, 70.4, 76.5, 70.5, 70.4, 70.6, 70.3, 73.9, 73.2	72	3.59

Table 2. Interfacial thickness determined by the modulus.

the statistical data of the interfacial thickness of the CF/PA-6 composite determined by modulus, the average interfacial thickness was 72 nm.

Adhesion and interphase thickness

Figure 11A presented the typical PF-QNM adhesion image of the interphase of the CF/PA-6 composite, the dark circle region was the carbon fiber with low adhesion, the lighter part around was the PA-6 with higher adhesion, and the boundary region between them was the interphase. To observe the change of the interfacial adhesion visually, the PF-QNM 3D adhesion image was displayed in Fig. 11B. It was apparent that the adhesion of the interphase increased abruptly from that of the carbon fiber to that of the PA-6. A radial scanning line from the carbon fiber to the PA-6 in Fig. 11A was taken to acquire the accurate adhesion data of the interphase of the CF/PA-6 composite, as displayed in Fig. 11C. What was remarkable in the figure was the sharp increased adhesion of the interphase. It was attributed to the special crystallization of the interphase and the changes of the RDF and energies. As red fitting curve shown in Fig. 11C, we defined the 90% of the width of the increasing adhesion region in the fitting curve as the interfacial thickness of the CF/PA-6 composite[33]. Table 3 summarized the statistical data of the interfacial thickness of the CF/PA-6 composite determined by adhesion, the average interfacial thickness was 72 nm.

In a word, the interfacial modulus and adhesion were distinct from those of the carbon fiber and PA-6, and the average interfacial thickness of the CF/PA-6 composite were 72 nm. It was consistent with the simulation

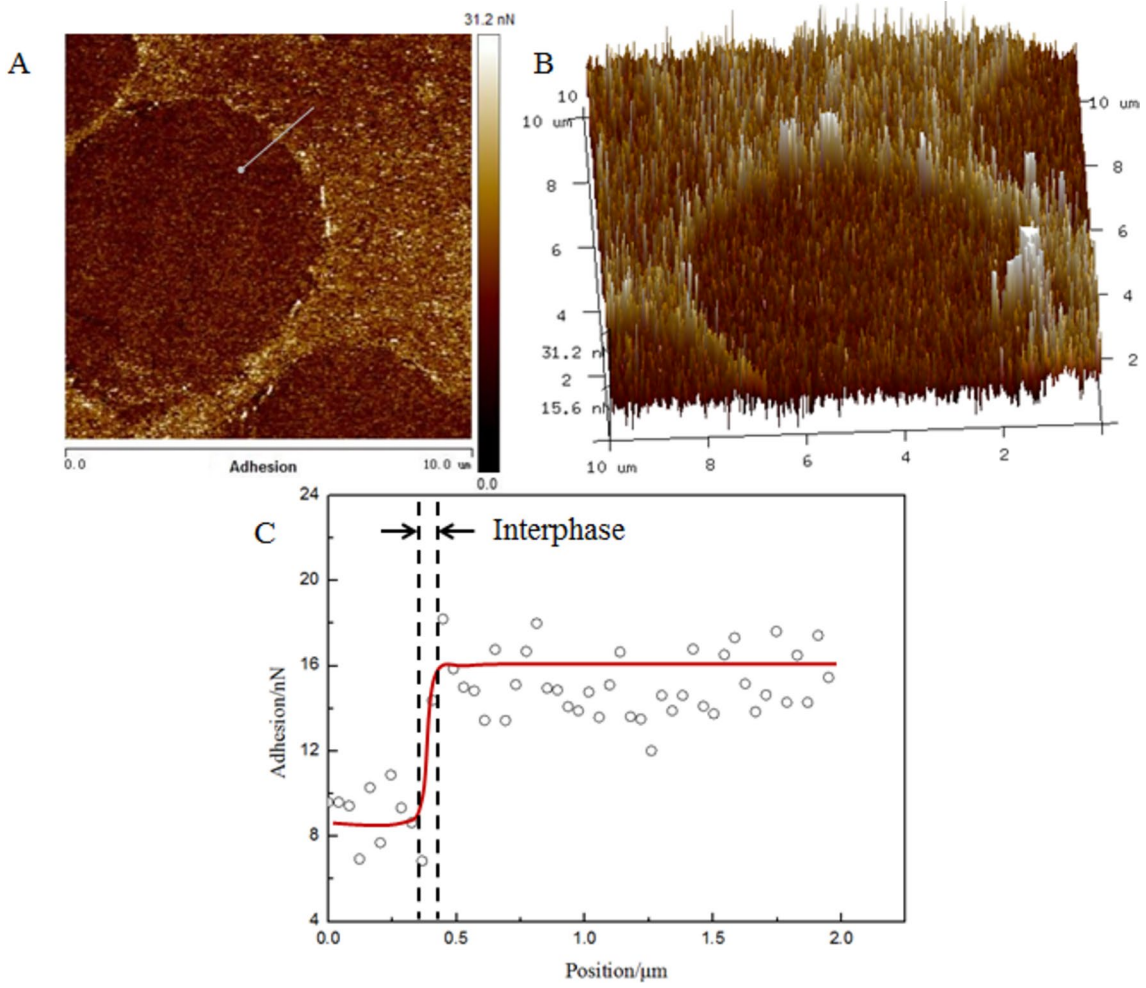

Figure 11. The typical PF-QNM adhesion image of the CF/PA-6 composite sample by hot pressing molding: (**A**) the PF-QNM adhesion image, (**B**) the PF-QNM 3D adhesion image, (**C**) corresponding data of the radial scanning line in (**A**).

	Interfacial thickness (nm)	Average (nm)	CV (%)
CF/PA-6 composite	79.3, 76.5, 71.9, 73.7, 73.0, 74.1, 70.4, 73.1, 72.6, 65.1, 72.4, 65.4, 68.6, 72.4, 68.4	72	5.29

Table 3. Interfacial thickness determined by the adhesion.

results. The adsorption and orderly folding of the PA-6 chains on the CF surface, the changes of the RDF and energies, all these led to the particular interfacial properties of the CF/PA-6 composite.

Conclusions

In order to provide a useful guide for the improvement of the interfacial properties, the investigation of the nanostructure and nanomechanical properties of the interphase in CF/PA-6 composite was necessary. In this study, MD simulation was carried out to directly display the absorption and regular folding of the PA-6 chains on the CF surface at the atomic level, presenting the crystallization of the interphase in the CF/PA-6 composite model. The changes of the radical distribution function, total energy, interfacial energy during the simulation time also revealed the interfacial crystallization in the CF/PA-6 composite model. At 2000 ps, the total energy and interfacial energy were lowest, thus the CF/PA-6 composite model reached a steady status and a well interaction between the PA-6 chains and CF surface. Then, the nanomechanical properties of the CF/PA-6 composite were investigated by AFM PF-QNM model. It was remarkable that the interfacial modulus sharply decreased and the interfacial adhesion keenly increased from those of the carbon fiber to those of the PA-6. The average interfacial thickness of the CF/PA-6 composite was 72 nm. In according with the simulation results, the interfacial properties were different from the properties of the carbon fiber and PA-6, attributing to the adsorption and orderly folding of the PA-6 chains on the CF surface and the changes of the RDF and energies.

Data availability

The datasets used and/or analysed during the current study available from the corresponding author on reasonable request.

Received: 8 June 2024; Accepted: 23 July 2024
Published online: 27 July 2024

References

1. Man, Z., Wan, B., Wang, H., Li, Q. & Chang, L. Experimental and numerical study on scratch performance of additively manufactured continuous carbon fibre reinforced polyamide 6 composites. *Compos. Sci. Technol.* **230**, 109314 (2022).
2. Shanmugam, V. *et al.* The mechanical testing and performance analysis of polymer-fibre composites prepared through the additive manufacturing. *Polym. Testing* **93**, 106925 (2021).
3. Wu, H. *et al.* Recent developments in polymers/polymer nanocomposites for additive manufacturing. *Prog. Mater. Sci.* **111**, 100638 (2020).
4. Li, N., Link, G. & Jelonnek, J. 3D microwave printing temperature control of continuous carbon fiber reinforced composites. *Compos. Sci. Technol.* **187**, 107939 (2020).
5. Penumakala, P. K., Santo, J. & Thomas, A. A critical review on the fused deposition modeling of thermoplastic polymer composites. *Compos. B* **201**, 100336 (2020).
6. Wang, P. *et al.* Preparation of short CF/GF reinforced PEEK composite filaments and their comprehensive properties evaluation for FDM-3D printing. *Compos. B* **198**, 108175 (2020).
7. Petrény, R., Almásy, L. & Mészáros, L. Investigation of the interphase structure in polyamide 6-matrix, multi-scale composites. *Compos. Sci. Technol.* **225**, 109489 (2022).
8. Sun, N. *et al.* Enhanced interfacial properties of carbon fiber/polyamide composites by in-situ synthesis of polyamide 6 on carbon fiber surface. *Appl. Surf. Sci.* **599**, 153889 (2022).
9. Zhang, Y. *et al.* Constructing a rigid-and-flexible twin-stage gradient interphase through starlike copolymer coating on carbon fibers: A route for enhancing interfacial properties of composites. *ACS Appl. Mater. Interfaces* **13**, 55633–55647 (2021).
10. Jiang, C., Zhang, J., Shaofeng, L., Ju, S. & Jiang, D. Effects of free organic groups in carbon nanotubes on glass transition temperature of epoxy matrix composites. *Compos. Sci. Technol.* **118**, 269–275 (2015).
11. Zhang, D., Chia, L. & Huang, Y. Effect of Carboxymethyl Cellulose (CMC) Functionalization on dispersion, mechanical, and corrosion properties of CNT/epoxy nanocomposites. *Chin. J. Polym. Sci.* **41**, 1277–1286 (2023).
12. He, M. *et al.* Establishing a phthalocyanine-based crosslinking interphase enhances the interfacial performances of carbon fiber/epoxy composites at elevated temperatures. *Compos. Sci. Technol.* **173**, 24–32 (2019).
13. Yang, C. *et al.* Electrothermally responsive self-healing for carbon fiber/epoxy interphase based on Diels-Alder adducts. *Compos. Sci. Technol.* **208**, 108767 (2021).
14. Salomão, G. R., Gojzewski, H., Erartsin, O. & Baran, I. Novel co-bonded thermoplastic elastomer-epoxy/glass hybrid composites: The effect of cure temperature on the interphase morphology. *Polym. Test.* **115**, 107736 (2022).
15. Wang, Y. *et al.* Understanding the graphene-polymer interfacial mechanical behavior via coarse-grained modeling. *Comput. Mater. Sci.* **222**, 112109 (2023).
16. Yazdanparast, R. & Rafiee, R. Investigating the influence of pull-out speed on the interfacial properties and the pull-out behavior of CNT/polymer nanocomposites. *Compos. Struct.* **316**, 117049 (2023).
17. Xuan, L. & Yihua, C. Multi-scale analysis of the interface structure and failure behaviors for n-SiO2@jute fiber/PP composites. *Compos. Struct.* **267**, 113865 (2021).
18. Prathumrat, P., Nikzad, M., Shireen, Z., Hajizadeh, E. & Sbarski, I. A combined experimental and molecular dynamic studies of curing of shape memory lignin-liquid crystalline elastomeric composites. *Compos. Sci. Technol.* **240**, 110099 (2023).
19. Yang, D., Sun, Y., Yang, Z., Chen, X. & Wang, C. Multiscale modeling of unidirectional composites with interfacial debonding using molecular dynamics and micromechanics. *Compos. Part Eng.* **219**, 108893 (2021).
20. Ahmed, K., Qin, X. & Yang, Y. Nanomechanical properties of sized and de-sized carbon fiber reinforced polypropylene composites. *J. Compos. Mater.* **58**(1), 13–24 (2023).

21. Wang, S. *et al.* Atomistic modeling of the effect of temperature on interfacial properties of 3D-printed continuous carbon fiber-reinforced polyamide 6 composite: From processing to loading. *ACS Appl. Mater. Interfaces* **15**, 56454–56463 (2023).
22. Nair, S. S., Wang, C. & Wynne, K. J. AFM Peakforce QNM mode for measurement of nanosurface mechanical properties of Pt-cured silicones. *Prog. Org. Coat.* **126**, 119–128 (2019).
23. Wei, W., Jian, C. S., Kwesi, S.-C. & Wenhui, D. Graphene oxide-reinforced thin shells for high-performance, lightweight cement composites. *Compos. Part B Eng.* **235**, 109796 (2022).
24. Niu, Y.-F., Wang, D.-D. & Yao, J.-W. Investigation of the performances for CFRP composites exposed to different aging environment at nano-scale. *Polym. Testing* **116**, 107771 (2022).
25. Baohe, W., Yan, N. & Jing, M. The effect of bioadhesive on the interfacial compatibility and pervaporation performance of composite membranes by MD and GCMC simulation. *J. Mol. Graph. Model.* **80**, 113–120 (2018).
26. Guo, S.-J., Yang, Q.-S., He, X. Q. & Liew, K. M. Modeling of interface cracking in copper-graphite composites by MD and CFE method. *Compos. Part B Eng.* **58**, 586–592 (2014).
27. Tang, Y. *et al.* Molecular dynamics simulation of adhesion at the asphalt-aggregate interface: A review. *Surfaces Interfaces* **44**, 103706 (2024).
28. Zhang, M. *et al.* Effects of CNT microstructural characteristics on the interfacial enhancement mechanism of carbon fiber reinforced epoxy composites via molecular dynamics simulations. *Thin-Walled Struct.* **195**, 111413 (2024).
29. Yang, H., Chen, Y., Liu, Y., Cai, W. S. & Li, Z. S. Molecular dynamics simulation of polyethylene on single wall carbon nanotube. *J. Chem. Phys.* **127**, 094902 (2007).
30. Pizzorni, M., Parmiggiani, A. & Prato, M. Adhesive bonding of a mixed short and continuous carbon-fiber-reinforced Nylon-6 composite made via fused filament fabrication. *Int. J. Adhes. Adhes.* **107**, 102856 (2021).
31. Yang, J. H., Hong, J. S., Lee, J. S., Sim, S. J. & Ahn, K. H. Rheological analysis of peroxide radical-induced modification of micro-algae-based polymer composite. *React. Funct. Polym.* **194**, 105803 (2024).
32. Qi, Y., Jiang, D., Ju, S., Zhang, J. & Cui, X. Determining the interphase thickness and properties in carbon fiber reinforced fast and conventional curing epoxy matrix composites using peak force atomic force microscopy. *Compos. Sci. Technol.* **184**, 107877 (2019).
33. Downing, T. D. *et al.* Determining the interphase thickness and properties in polymer matrix composites using phase imaging atomic force microscopy and nanoindentation. *J. Adhes. Sci. Technol.* **14**, 1801–1812 (2000).
34. Kangyi, L. *et al.* Enhanced longitudinal compressive strength of CFRP composites through matrix stiffening via flexible/rigid epoxide grafted silica: A combined analysis of simulation and experiments. *Compos. Part B Eng.* **235**, 109756 (2022).
35. Tian, C., Cui, J., Ning, N., Zhang, L. & Tian, M. Quantitative characterization of interfacial properties of carbon black/elastomer nanocomposites and mechanism exploration on their interfacial interaction. *Compos. Sci. Technol.* **222**, 109367 (2022).

Acknowledgements

We acknowledge the College of Aerospace Science and Engineering of National University of Defense Technology and the materials studio soft by Accelrys Inc for providing computational resource. This work was supported by the National Natural Science Foundation of China under Grant No. 52303115.

Author contributions

Yixin Qi: Funding Acquisition, Investigation, Methodology, Resources, Validation, Writing-Original Draft, Writing-Review Editing. Dazhi Jiang: Conceptualization, Funding Acquisition, Project Administration. Su Ju: Project Administration, Software, Supervision. Jianwei Zhang: Supervision.

Competing interests

The authors declare no competing interests.

Additional information

Correspondence and requests for materials should be addressed to Y.Q.

Reprints and permissions information is available at www.nature.com/reprints.

Publisher's note Springer Nature remains neutral with regard to jurisdictional claims in published maps and institutional affiliations.